TU DELFT

Investigation of pore evolution in concrete by spin-echo small angle neutron scattering

by

Caspar Boers

Bachelor Thesis

13 October 2017

Abstract

A concept for the geological repository of nuclear waste in the Netherlands incorporates concrete barriers in a Boom clay environment. An understanding of the pore evolution within this concrete may help predict changes in the materials physical strength and transport properties. Techniques that are currently used for this purpose include Mercury Intrusion Porosimetry (MIP), Focused Ion Beam Scanning Electron Microscopy (FIB-SEM), Broad Ion Beam Scanning Electron Microscopy (BIB-SEM), Micro Computer Tomography (micro-CT), Quasi-Elastic Neutron Scattering (QENS), Small Angle Neutron Scattering (SANS) and Small Angle X-ray Scattering (SAXS). In an effort to investigate the pore evolution in concrete that chemically interacts with its environment, these techniques could be complemented by new methods. A promising technique is Spin Echo Small Angle Neutron Scattering (SESANS). This technique exploits the scattering of neutrons from a sample causing a difference in Larmor precession angle when the transmission angle changes. The practical applicability of this technique on concrete, as well as the extent to which the measured polarization can be related to pore evolution are investigated in this study. Especially, the contribution of refraction to the overall polarization has been examined by comparing the polarization in quartz, concrete's main constituent, to a model for neutron refraction in cylindrical wires. Because at the size scale of the quartz particles, refraction rather than diffraction is the dominant phenomenon when neutrons are considered. The modelling involved an analysis of the effect of the number of layers of quartz particles in concrete. The results showed that neutron refraction significantly contributes to the measured signal and thus should be taken into account in further quantitative analysis. The results are based on a model for well-oriented cylindrical wires of the same size, whereas quartz particles are amorphous and anisotropically oriented and vary largely in size. To gain more detailed information on the contribution of

neutron refraction to the polarization a model must be developed that accounts for these anomalies.

Contents

Chapter 1

Introduction

Nuclear waste is produced mainly in nuclear power plants for electricity production, but also in important applications of radiation in health care, industry, agriculture and research. Nuclear waste is hazardous to living organisms due to the ionizing radiation that it emits, and remains so for periods of hundreds of thousands of years. Because of this long period of hazardous activity, preventing future generations from exposure to this ionizing radiation has become a major scientific and technical challenge. Current policy in the Netherlands is that radioactive waste is collected, treated and stored by COVRA (Centrale Organisatie Voor Radioactief Afval), which is the only company in the Netherlands that is qualified to do this. After interim storage for a period of at least 135 years, radioactive waste is designated to be emplaced in deep underground facilities. There is a world-wide consensus among scientist and engineers that such geological repositories represent a safe disposal option for radioactive waste [1]. This thesis is conducted in the context of OPERA (OnderzoeksProgramma Eindberging Radioactief Afval), which is the third Dutch research programme on geological disposal of radioactive waste and lasted from 2011 to 2016.
In this programme, Boom clay is investigated as a host rock for the facility and cementitious materials are used to provide mechanical support, enclosure of emplaced waste and containment. An impression of what this concept will come to look like is depicted in Fig. (1.1).

Species in the Boom clay pore water, in particular its main compounds sulfate and chloride, interact with concrete and are likely to cause degradation. It has been widely recognized that the pore structure of concrete is an excellent indicator of the

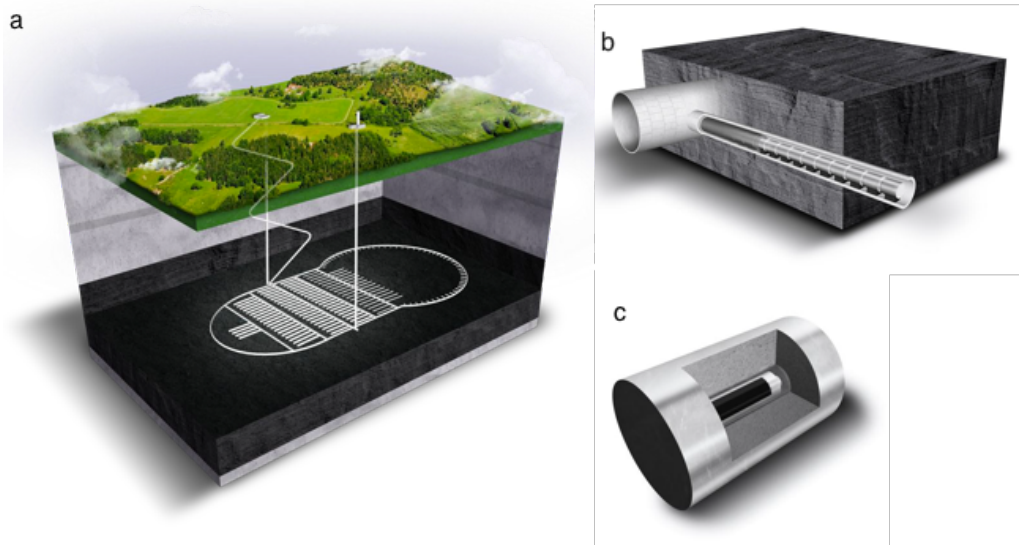

FIGURE 1.1: **Artist impression of the OPERA geological repository concept for the disposal of radioactive waste in a concrete structure with Boom clay as host rock.** After [2]. **a** The conrete structure (white) in Boom clay (anthracite) deep below the earth's surface. **b** Enlargement of a section of the repository where OPERA supercontainers will be stored. **c** This *supercontainer* is designed For the storage of heat generating High Level Waste (HLW). It has a core of heat generating HLW, surrounded by concrete in a steel envelope.

material's main characteristics, such as physical strength and transport properties [3]. Therefore this thesis aims to investigate how porosity in concrete evolves over time during these degradation processes. Renowned techniques such as Mercury Intrusion Porosimetry (MIP), Focused Ion Beam Scanning Electron Microscopy (FIB-SEM), Broad Ion Beam Scanning Electron Microscopy (BIB-SEM), Micro Computer Tomography (micro-CT), Quasi-Elastic Neutron Scattering (QENS), Small Angle Neutron Scattering (SANS) and Small Angle X-ray Scattering (SAXS) exist for the investigation of the pore structure of concrete. But many involve the intrusion of liquid or gas, and thereby change the characteristics of the pore system. Other techniques such as QENS, SANS and SAXS make use of fields or irradiation with elementary particles and are more sophisticated in the sense that they don't alter the sample characteristics.

The goal of this thesis is to evaluate Spin-Echo Small Angle Neutron Scattering as a potential measurement method for the investigation of pore evolution in concrete. SESANS has been applied succesfully to gels, biological systems, proteins and powders. The durability of concrete is reviewed with a focus on chemical degradation mechanisms such as leaching, sulfate attack and chloride ingress. Furthermore, the pore structure of concrete and the main experimental methods to investigate it

are considered. After all relevant characteristics of concrete have been put forward an explanation of the SESANS technique is given. Special attention is devoted to the subject of neutron refraction.

Chapter 2

Literature Review

In the OPERA geological repository concept, the concrete structure will be embedded in Boom clay. In this chapter the main chemical processes that will occur in this environment will be discussed.
Chemical degradation is defined by Seetharam and Jacques [4] as "the gradual change in pore-water composition and concrete mineralogy, usually characterized by a decreasing Ca/Si ratio and a decreasing pH". In deep geological disposal facilities hosted in Boom clay the concrete is affected by constituents of Boom clay pore water.

2.1 Boom Clay pore water

Boom Clay is a clayrock, i.e.: a fine-grained, low permeable material with a significant amount of clay minerals [5]. Naturally occurring in parts of the Netherlands and Belgium it owes its name to a little town in Belgium called Boom. Boom Clay has a variated mineralogy with quartz, pyrite and clayey minerals (illite, kaolinite or feldspars). Several properties make Clay a desirable host formation for radioactive waste disposal. Among these are its low permeability and low hydraulic gradients; chemical buffering capacity; propensity for plastic deformation and self-sealing of fractures; geochemical characteristics that favour low solubility of radionuclides; and high capacity to retard the migration of radionuclides towards the accessible environment, e.g. through sorption capacity and due to a diffusion-dominated transport [6]. Taking into account its abundant presence at safe depths in the ground of large parts of the Netherlands, Boom Clay is assigned

as hostrock for the concept for geological disposal of nuclear waste [7]. The clay will act as a natural barrier between the repository and biosphere by retarding migration of radionuclides and any other hazardous substances that over geological times might eventually escape form the repository.
At the boundary between the deep geological facility and host rock the interaction with Boom Clay porewater leads to concrete deterioration. The main criteria characterizing the potential harm of ground water to Portland cement hydration products are: composition of impurities; pH; mineralization; and water hardness. The pore water in the Boom Clay at Zeeland, the Netherlands, is found to be mildly alkaline with an in situ pH value of about 7.4-8.2 [8]. The redox potential is integral part of the pore water chemistry in the host formation. Pore water chemistry is of central interest when evaluating the evolution of the engineered barriers and the retention of any escaping radionuclides. Pore water chemistry and mineralogy affect, among other things, the sorption and retardation potential of the host formation (NAGRA, 2010) [9]. The Boom Clay pore water has a multi-elemental composition including cations (Al3+, Ca2+, Mg2+ etc.) and anions (Cl-,F-, SO42- etc.) [7]. Over time, these elements may affect the chemical composition of the concrete, generating hyper alkaline environment. Since chlorides and sulfates are its main components this chapter discusses the processes leaching, sulfate attack and chloride ingress.

2.2 Leaching

In general, leaching is the process of extracting substances from a solid by dissolving them in a liquid. Since concrete pore water conditions are high alkaline for a long period of time, the external ground water will almost always be relatively acidic. So, when ground water encounters a concrete surface, Ca^{2+} and OH^{-} ions are removed from the concrete and dissolved in the pore water. This process, which is sometimes more specifically referred to as *lime leaching*, enlarges the pore system of the concrete and thus locally increases it's permeability. Three generalized areas where leaching takes place can be distinguished: (1) from free surfaces on the concrete, (2) from the surface of cracks in the concrete and (3) from the interior of the concrete that is porous, lean and pliable [10]. The hydration product that is most severely affected by leaching is $Ca(OH)_2$ (Portlandite), because of it's high solubility and abundant presence. Also, Porlandite mainly occurs in concrete

as large crystals whose dissolution leaves macroporosity. In a lower degree Ca^{2+} is also leached away from the C−S−H, C_3A and C_4AF phases. The decalcification of C-S-H however leaves microporosity, which has a less catastrophic effect on the compressive strength of the concrete [11]. Some of the most common leaching reactions involving cement hydration products and aggregate materials are given below. In these formulas HA represents monoprotonic acid. For calcium hydroxide the general reaction occurs at a pH value of below 12.6:

$$\mathrm{Ca(OH)_2 + 2\,HA \longrightarrow CaA_2 + 2\,H_2O.} \tag{2.1}$$

For ettringite the general reaction occurs at a pH value of below 10.7:

$$\mathrm{6\,CaO \cdot Al_2O_3 \cdot 3\,SO_3 \cdot 32\,H_2O + 6\,HA \longrightarrow 3\,CaA_2 + 2\,Al(OH)_3 + 3\,CaSO_4 + 32\,H_2O} \tag{2.2}$$

In the case of CSH gel, the reaction (which occurs below a pH value of $\tilde{1}0.5$:

$$\mathrm{\mathit{x}CaO \cdot \mathit{y}SiO_2 \cdot \mathit{n}H_2O + 2\,\mathit{x}HA \longrightarrow \mathit{x}CaA_2 + \mathit{y}Si(OH)_4 + (\mathit{x} + \mathit{n} - 2\,\mathit{y})\,H_2O,} \tag{2.3}$$

where $Si(OH)_4$ is an amorphous silica gel. For calcium aluminate hydrates, such as monosulphate, the general reaction is:

$$\mathrm{3\,CaO \cdot Al_2O_3 \cdot CaSO_3 \cdot 12\,H_2O + 6\,HA \longrightarrow 3\,CaA_2 + 2\,Al(OH)_3 + CaSO_4 + 12\,H_2O} \tag{2.4}$$

The leaching depth over a certain amount of time depends on the aggressiveness of the external water (the lower the pH the higher the aggressiveness) and the transport properties of the concrete, which are mainly determined by the microstructure [12]. From studies by Lagerblad [13] and Yokozeki et al. [14] we know that leaching is a slow process, but it does become significant when regarding timescales that are encountered in deep repository. The main consequences of leaching and decalcification are threefold:

- An increase in total porosity that causes a change of the transport properties in concrete.
- The disappearance of calcium from the concrete leads to a decrease of the mechanical strength.
- The composition of the solid phase and the pore water of the concrete are subject to change along with the pH and other geochemical properties [15].

The increased porosity caused by leaching and decalcification could be counteracted by a secondary effect called porosity clogging. To predict the effect of the highly alkaline pore fluid conditions caused by the cementitious materials on clayey barriers several modelling studies on large time scales have been carried out. Research either focus on purely thermodynamic models [16] [17] or on combined thermodynamic/kinetic models [18] [19]. Each of these models predits a porosity-clogging behaviour that should mitigate the mass transport. Furthermore, Liu et al. [20] developed a parallel coupled model for interaction between concrete and clay, in the context of Belgian deep disposal study. They conclude that the precipitation of calcite is the main reason for clogging. Furthermore, Song et al. [21] showed that leaching can greatly change the internal chemical environment and the microstructure of cement pastes, thereby changing the chloride diffusion behavior and degrading the chloride-ingress resistance.

2.3 Sulphate attack

Sulfate attack is a process whereby sulfate ions in solution chemically react with compounds present in hydrated cement [22]. Roughly three different mechanisms may be incurred: extensive cracking, expansion and decomposition of aggregate and cement paste. Therefore, the overall effect is loss of concrete strength [23]. The chemistry of sulfate attack comprises plentiful imbricated reactions. This gives rise to a complexity which makes a conclusive definition of sulfate attack difficult. In this thesis the artificial distinction [24] between chemical and physical sulfate attacks will be avoided. However, there is a fundamental distinction between internal and external sulfate attack [25].

2.3.1 Internal sulfate attack

Internal sulfate attack is caused by a soluble source that is consolidated in the concrete during the mixing process. In practice this occurs with the formation of ettringite after hydration of the cement and therefore, internal sulfate attack is also referred to as delayed ettringite formation. Since this internal sulphate attack can easily be avoided by taking simple measures concerning the choice of cement, it is not further considered in this thesis.

2.3.2 External sulfate attack

Reference is made of external sulfate attack when sulfate propagates into the material and modifies transport and mechanical properties [26]. The ingress of sulphate ions then causes an external sulphate attack on cement-based materials, leading to an uptake of sulphates into the cement micro-structure [27]. This is likely to happen at the boundary of concrete with Boom Clay pore water. The composition and micro-structure of the concrete is changed in a region with a well-defined boundary which is called the reaction front.
In the realm of external sulphate a distinction can be made between ettringite sulphate attack (ESA) and thaumasite sulphate attack (TSA). The former can be limited by the choice of cements with an amount of C_3A lower then 3%, whereas for the latter sources of SO_4^{2-}, CO_3^{2-} and SiO_3^{2-} should be limited and temperatures below 15°C should be avoided (because thaumasite forms preferentially at temperatures lower than 15°C) [28].

The main expansion as a manifestation of external sulfate attack due to the formation of ettringite takes places according to the following chemical reaction:

$$\mathrm{C_4A\overline{S}H_{12} + 2\,C\overline{S}H_{12} + 16\,H \longrightarrow C_6A\overline{S}_3H_{32}} \tag{2.5}$$

In Portland cement with calcium silicate based binders another reaction occurs that applies to internal as well as external sulfate attack. The C_3A then provides aluminate for the ettringite to form as:

$$\mathrm{C_3A + 3\,C\overline{S}H_2 + 26\,H \longrightarrow C_6A\overline{S}_3H_{32}} \tag{2.6}$$

In the following several conditions that have to be met to produce expansion are discussed. First, a certain threshold of ettringite molecules must be exceeded to generate pressure on adjoining solids. Second, the ettringtie must be formed in a locally confined chemical reaction [29]. Third, the ettringite must be formed after the cement paste had set to generate expansion.

As sulfate ions enter the cement paste by means of an external sulfate attack and react with the calcium hydroxide present in the cement paste gypsum may be formed:

$$\mathrm{{SO_4}^{2-} + Ca(OH)_2 + 2\,H_2O \longleftrightarrow CaSO_4 \cdot 2\,H_2O + 2\,OH^-} \tag{2.7}$$

There is no general agreement among researchers about whether or not this reaction leads to expansion of the cement paste. Tian [30] and Cohen [31] concluded that gypsum formation may cause expansion. However, Mather investigated that gypsum forms primarily, if not exclusively, by reaction of sulfate ions with calcium ions and precipitation of gypsum from a solution that by evaporation, becomes supersaturated [32].

Thaumasite may be formed in Portland cement based concretes in specific circumstances, i.e. abundat presence of sulfate and carbonate ions, low temperatures and alkaline conditions [33]. The chemical reaction can be expressed as:

$$3\,Ca^{2+} + {SiO_3}^{2-} + {CO_3}^{2-} + {SO_4}^{2-} + 15\,H_2O \longrightarrow 3\,CaO \cdot SiO_2 \cdot CO_2 \cdot 15\,H_2O \quad (2.8)$$

Contact with sulfate-containing ground water remains the most common cause of the thaumasite form of sulfate attack in bruied concrete [34].

2.4 Chloride ingress

Chloride ingress is the process of penetration and redistribution of chloride in concrete. Just like with sulphate, as discussed in the previous paragraph, the chloride either is present in the cement itself or comes from external sources. Since commercial cement only contains chloride up to 0.01wt% [35], groundwater will be the main source. Through diffusion the chloride ions penetrate into the concrete pore water [36]. These are encountered in concrete both as free ions in the pore interstitial solution, and as chemically bound component of hydrate phases. Out of these appearances, the free chloride ions are the most dangerous because of their capacity to diffuse further into the concrete and in some cases even towards the steel reinforcement bars [37].
Many literature review articles [22] [38] [39] in this field link chloride ingress directly to steel corrosion rather than considering it as a chemical degradation process [4].

2.4.1 Formation of Friedel's salt

Friedel's salt, also referred to as hydrocalumite, has the general formula $[Ca_2Al(OH)_6]Cl \cdot 2\,H_2O$. Among cement chemists it's customary to use the formula $3\,CaO \cdot Al_2O_3 \cdot CaCl_2 \cdot 10\,H_2O$ instead. The similitude of both formulas can be understood by considering that

$$2\,OH^- \rightleftharpoons O^{2-} + H_2O \tag{2.9}$$

and doubling the stoichiometry of the first formula. Friedel's salt is ranked among the layered double hydroxides (LDH), which is an important class of materials for environmental remediation applications [40] and it's structure is discussed by Filippakis et al [41].

Essentially, two mechanisms have been proposed [42]. On the one hand there is the adsorption mechanism. In this case Friedel's salt forms due to the adsorption of the bulk Cl^- ions present in the pore solution into the interlayers of the principal layers, $[CaAl(OH^-)_6 \cdot 2\,H_2O]^+$, of the AFm structure to balance the charge. On the other hand there is the anion-exchange mechanism. In this case a fraction of the tree-chloride ions bind with the AFm hydrates to form Friedels salt by an anion-exchange with the OH^- ions present in the interlayers of the principal layer, $[Ca_2Al(OH^-)_6 \cdot nH_2O]^+$.

Friedels salt has an important role in the cement chemistry of deep geological repositories where concrete is used as sealing material [43]. That is partly due to Friedel's salt being more stable than the hydroxy aluminate AFm. Furthermore, the AFm phases retard chloride ingress by binding the chlorides. This is due to the property of AFm phases exhibiting anion exchange [44].

Chapter 3

Pore Structure in Concrete

As the aim of this research is to investigate pore evolution, understanding of the pore structure in concrete is essential. This chapter discusses the range of pores that are encountered in concrete and several experimental techniques to probe them. There is concencus among researchers that that the pore structure of concrete strongly influences its mechanical behavior as well as its transport properties and could accordingly be regarded as one of the most important characteristics [3]. Therefore, the mapping of this pore structure is often pursued in research. But the large range of pore sizes (nanometer to micrometer scale [45]) demands the use of multiple measurement techniques for characterization. Moreover, many techniques require the samples to be dried in a pretreatment, thereby generating important damages for the materials microstructure in the capillary porosity domain [46].

3.1 Classification of the pores

Practically distinction is made between the larger pores between cement grains (capillary pores) and the internal porosity of the C-S-H gel (gel pores). More specifically, Mehta [47] states that five types of pores occur in concrete:

- Gel pores, which are micropores of characteristic dimension 0.510 nm.
- Capillary pores, which are mesopores with average radius ranging from 5 to 5000 nm.

- Macropores due to deliberately entrained air.
- Macropores due to inadequate compaction.
- Cracks at aggregatemortar interface due to shrinkage.

it should be emphasized that the pore sizes are continuously distributed; i.e. the pore sizes of capillary pores and gel pores could overlap. The most important parameter concerning the pore system is the specific surface area. This is the area of the interface between solid phases and the pore system per unit amount of material. More on various measurements methods that probe this characteristic can be read in paragraph 3.2. Other parameters are the total porosity and the pore size distribution.

3.2 Experimental techniques for characterizing the pore system

When it comes to experimental techniques for characterizing the pore system, on the one hand there are techniques that require the intrusion of a fluid or a gas into the pore system [48] and on the other hand there are techniques that use irradiation or fields to probe the material [49]. A downside to the intrusion techniques is that samples need to be dried, thereby altering the pore structure and possibly also other characteristics of the concrete. The latter category, however, demands expensive equipment and features complex data interpretation.

3.2.1 Techniques using irradiation or fields to probe the material

Nuclear Magnetic Resonance probes the response of materials to an oscillating magnetic field. It's a renowned technique for determining the structure of organic compounds. When applied on cement-based materials it exploits the fact that nuclear spin interactions between water and the solid pore walls are much stronger than interactions in the bulk fluid. Thereby it's provides quantitative and structural information on the anhydrous and hydrated phases of Portland cement and details about the porosity, pore size distributions, and interconnectivity

of cement-based materials [50] [51] [52].

Quasi-Elastic Neutron Scattering (QENS) is based on inelastic neutron scattering and exploits the measured resulting energy transfer to investigate diffusion in solids. As discussed in the identification of function and state of water at the nanoscale in concrete is a complex issue. QENS can be used to discern between the different states summarized in [53].

Small-Angle Scattering (SAS) is based on the diffraction of collimated beams of radiation after interaction with structures. Structures larger than the wavelength of the radiation can be probed. **SAXS** and **SANS** utilize the scattering of X-rays and neutrons respectively. Neutrons are scattered by interactions with atomic nuclei, while X-rays are scattered by interactions with outer shell electrons. When applied to concrete these techniques yield direct data on particle morphology, surface area, and pore size distribution. Also, they allowed Jennings to develop a model for the nanostructure of C-S-H based on the interpretation of water sorption isotherms [54].

Chapter 4

Spin-Echo Small Angle Neutron Scattering

In this research spin-echo small angle neutron scattering (SESANS) is used to explore the pore structure of concrete samples. SESANS is one of many techniques that is based on elastic neutron scattering. Another, more established, technique is small angle neutron scattering (SANS). However, SANS probes structures in the range of $1nm$ – $100nm$. It is therefore a useful technique for studying gel pores in concrete. But the sizes of capilarry pores in concrete ($5nm$ – $5\mu m$) are often well beyond these limits. For the investigating capilarry pores in concrete there advantages of using SESANS instead of SANS:

- There is no need for high intensity because collimation is not needed
- Multiple scattering effects are easily accounted for [55].
- It allows structures in the range $5nm$ - $20\mu m$ to be studied. This length scale corresponds to the pore sizes of interest.

In order to understand SESANS one first must become acquainted with the principles of neutron scattering and neutron spin-echo. The following text provides a brief review of these principles.

4.1 Neutron Scattering

Free neutrons are electrically neutral and have half-integer spin. These properties imply that neutrons can have nuclear and magnetic interactions with materials. Suppose a beam of neutrons characterized by wave vector $\mathbf{k}_i$ falls on a sample as depicted in Figure 4.1. The neutrons are then scattered along direction $\hat{\boldsymbol{k}}_{\boldsymbol{f}}$ or they traverse through the sample without any interaction. The extent to which neutron scattering occurs in a material is determined by its Scattering Length Density (SLD). The SLD value of a material depends on how tightly packed the scattering entities are and the intrinsic scattering power of these scattering entities. Since nuclear and magnetic interaction probabilities (or *cross sections*) are both small, a neutron can usually penetrate well into the bulk of the specimen under investigation[56]. Therefore neutron scattering techniques are used to investigate the structural information of bulk samples [56]. Generally this structural information can be extracted from either the scattered or the transmitted beam, depending on the specific technique.

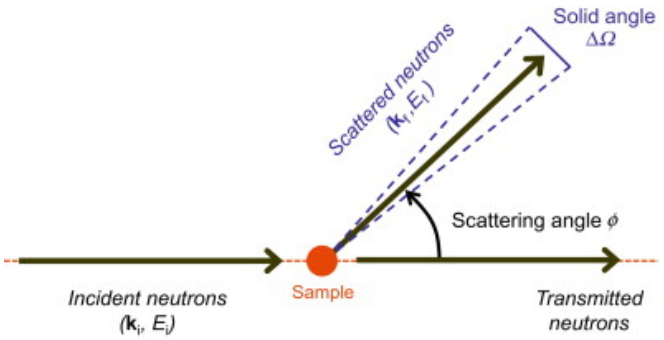

FIGURE 4.1: **Schematic diagram of a generic arrangement for neutron-scattering experiments** After [57]. Here $\boldsymbol{k}$ represents the wavenumber of the neutron and $\boldsymbol{E}$ the energy. The solid angle $\boldsymbol{\Delta\Omega}$ is the two-dimensional angle in three-dimensional space that the sample subtends at a point.

4.2 Neutron Spin Echo (NSE)

In neutron spin echo, the Larmor precession in magnetic fields before and after the scattering are compared to find the velocity change of neutrons that have traversed a sample [58]. This section describes how this comparison is established. Larmor precessions of a particle are changes in orientation of the rotational axis of its magnetic moment about an external magnetic field [59]. Polarized neutrons in the

incoming beam have different velocities which are encoded as precession angles by an external magnetic field. Subsequently an equal and opposite magnetic field is applied that exactly compensates the accumulated precession angle and realizes an echo of all neutron spins [60]. When there is no sample in between the precession regions the polarization will be fully restored at the end of this process. The presence of a sample, however, causes scattering which changes the velocity of part of the neutrons. This leads to a loss of polarization that is proportional to the distribution in spin-echo time, which is the time neutrons spend traveling through both precession regions. Thus in neutron spin-echo the correlation function is measured as a function of spin-echo time [61].

4.3 Eigenstate Shifter

The phenomena discussed above are applied in the semi-quantum mechanical explanation of the SESANS technique. In Figure 4.2 a precession region with tilted interfaces and a magnetic field perpendicular to the polarisation of the incoming neutron beam is depicted. In this setup the neutron beam can be considered to consist of two spin-states: one parallel- and one anti-parallel to the external magnetic field. Inside the precession region these eigenstates are split due to an increase or decrease in potential energy respectively. It is important to note that splitting only occurs in the direction normal to the magnetic field boundary. All superpositions of the neutron beam leave the precession region in a direction parallel to the incombing beam but they have been shifted in the $\boldsymbol{z}$-direction. The seperation in the direction perpendicular to the neutron path is the spin-echo length [61], which can be expressed as

$$\boldsymbol{z = \frac{c\lambda^2 LBtan(\theta_0)}{2\pi}} \tag{4.1}$$

where $\boldsymbol{c = 4.632 \times 10^{14} T^{-1} m^{-2}}$ is the Larmor precession constant and $\boldsymbol{\lambda}$ is the neutron wavelength and the remaining parameters are explained in the caption of Figure 4.2. From equation 4.1 it follows that the spin-echo length can be modified by varying any of the parameters determining its value.

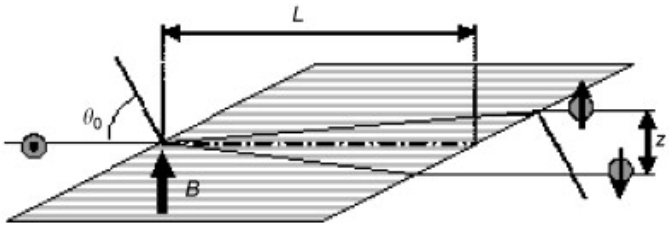

FIGURE 4.2: **A schematic side view of a precessioin device shifting the eignestates of the incoming neutron beam**. After [61]. The precession region is depicted by the hatched area. Here $\boldsymbol{z}$ is the spin-echo length, $\boldsymbol{L}$ is the length of the precession region, $\boldsymbol{B}$ is the strength of the magnetic field and $\boldsymbol{\theta_0}$ is the angle between foil and incoming beam.

4.4 SESANS in Delft

This section describes the SESANS instrument that is installed at the reactor institute in Delft and which is used for the measurements is this thesis. The device depicted in Figure 4.2 is mounted twice with opposing magnetic fields as discussed in Section 4.2 to form the setup shown in Figure 4.3. Small-angle scattering occurs only at gradients in the scattering length density [61], i.e.: at positions of inhomogeneities in the sample. A neutron spin-echo length that exceeds the SLD results in a difference in final spin orientation that can be measured as the depolaristaion of the beam.

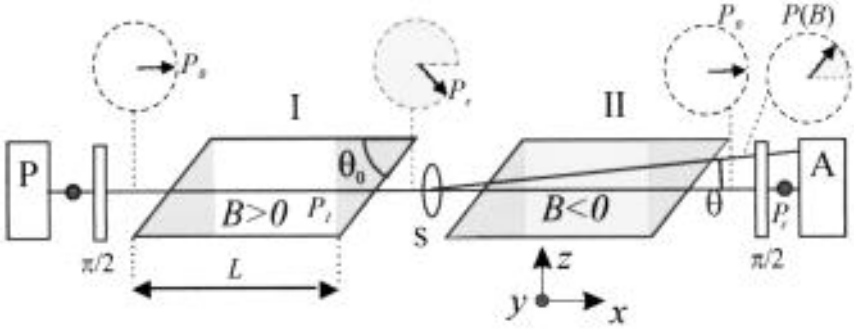

FIGURE 4.3: **Schematic of the spin-echo small angle neutron scattering procedure.** After [62]. The circles in the top of the figure represent the precession angle at different positions in the setup. In the polarizer (P) the neutron beam is polarized. Then it is rotated over $\boldsymbol{\pi/2}$ to $\boldsymbol{(x, z)}$ in alignment with the first precession region (see Figure 4.2). The shadowed areas cause the inclination effect. At the sample (S) scattering occurs and the proceding beam is a superposition of neutrons with different precession angles. The neutrons are rotated over $\boldsymbol{\pi/2}$ and then they may pass through the analyzer (A) to be detected.

4.5 Measured Quantities

Through the transmission of polarization SESANS measures $\boldsymbol{G(z)}$, the projection of the autocorrelation function of the density distribution, for which the expression is derived in [63]. Another important measure is the average number of times a neutron scatters when traversing a sample, which for a two-phase system is expressed as

$$\boldsymbol{\Sigma_t = \lambda^2 t(\Delta_{\rho 0})^2 \phi(1-\phi)\xi,} \tag{4.2}$$

where t is the thickness of the sample, $\boldsymbol{\lambda}$ is the neutron wavelength, $\boldsymbol{\phi}$ is the packing fraction and $\boldsymbol{\xi}$ is the correlation length of the sample inhomogeneities and $\boldsymbol{\Delta_{\rho 0}}$ is the scattering length density between the two phases. The raw data generated by SESANS measurements is the polarization as a function of the parameters mentioned above

$$\boldsymbol{P(z) = P(0) exp(\Sigma_t[G(z) - 1]).} \tag{4.3}$$

Normalization with the empty beam polarization gives $\boldsymbol{P(0) = 1}$. As the spin-echo lengths increases it exceeds the length scale of characteristic sample inhomogeneities, i.e.: $\boldsymbol{G(\infty) = 0}$. This insight enables us to compute the fraction of neutrons that does not scatter when traversing the sample referred to as the saturation level of measured polarization:

$$\boldsymbol{P(\infty) = exp(-\Sigma_t),} \tag{4.4}$$

4.6 Data Interpretation

Since in SESANS the polarization is a function of the spin echo length in *real-space*, an intuitive interpretation of measurements is possible [63]. In Figure 4.4 a standardized plot for a generic SESANS measurement is given. For very small spin-echo lengths the polarization is equal to the empty beam polarization so the graph starts at a value of 1 ($\boldsymbol{P(0) = 1}$). The polarization then decays for increasing spin-echo length and finally saturates at a spin-echo length equal to the characteristic length for the examined sample. The value of $\boldsymbol{l_{max}}$ indicates the point at which no more density correlations are seen in the sample [63]. The height of the polarization at saturation level can be computed from Equation 4.4 and the difference between the empty beam polarization and the polarization at

saturation level can be computed by substituting Equation 4.2 into $\mathbf{1 - P(\infty)}$. The saturation level depends on chemical composition $\boldsymbol{\Delta_{\rho 0}}$, packing fraction $\boldsymbol{\phi}$ and correlation length $\boldsymbol{\xi}$ of the sample inhomoginities. Therefore the saturation level can be exploited to find $\boldsymbol{\xi}$, which can be conceptually interpreted as the average length of all lines possibly drawn inside the density fluctuations [63].

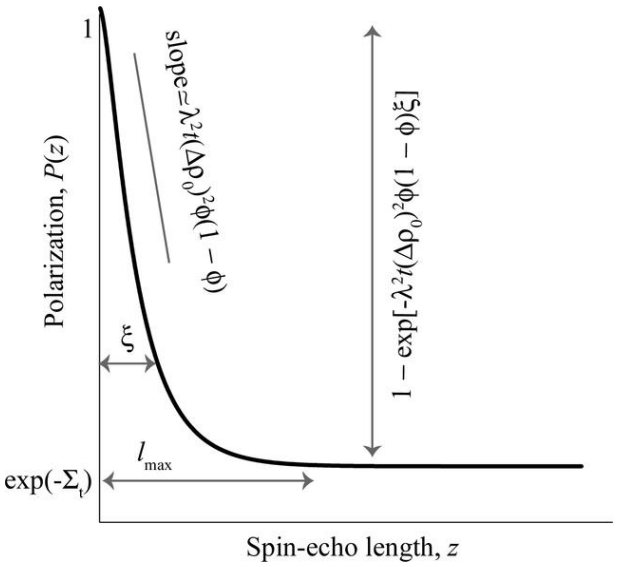

FIGURE 4.4: **Generalised graph of a SESANS measurement.** After [64]. This is a measurement of dilute isotropic materials without any ordering. The polarization is plotted against the spin-echo length.

For neutron propagation substances with particle sizes of $50\boldsymbol{\mu m}$ and larger the phenomenon of refraction becomes dominant over diffraction. As concrete contains large amounts of quartz particles which often have grain sizes in the $\boldsymbol{mm}$ regime, refraction is a phenomenon to consider.

4.7 Neutron refraction

Plomp et al. [65] have measured the effect that refraction of cylindrical wires has on instrumentation sensitive to SANS. They demonstrated that refraction causes an angular distribution in the neutron beam. This angular distribution can be expressed quantitatively as:

$$\boldsymbol{I(\theta) = \frac{1}{4\delta} \frac{1}{\left(1 + (\theta/2\delta)^2\right)^{\frac{2}{3}}}} \tag{4.5}$$

where $\boldsymbol{\theta}$ is the deviation between incoming and outgoing beam and $\boldsymbol{\delta}$ is related to the refractive index as:

$$\boldsymbol{n = 1 - \delta = 1 - \frac{\rho \lambda^2 \bar{b}}{2\pi}} \tag{4.6}$$

and where $\boldsymbol{\rho}$ is the number of nuclei per unit volume, $\boldsymbol{\lambda}$ is the wavelength and $\boldsymbol{\bar{b}}$ is the mean coherent scattering length, which can be defined as the $\boldsymbol{SLD}$ divided by the atomic density. The refractive index $\boldsymbol{n}$ can be regarded as a ratio between the propagation rate of the neutron in two different media. In the simplest case, one of the media is the vacuum, for which the refractive index is equal to $\mathbf{1}$, resulting in the formula:

$$\boldsymbol{n = \frac{c}{v}} \tag{4.7}$$

The relative refractive index between two media can then be calculated as:

$$\boldsymbol{n_{1\to 2} = \frac{v_1}{v_2} = \frac{c/n_2}{c/n_1} = \frac{n_2}{n_1}} \tag{4.8}$$

Allen et al. [66] have shown that the density of C–S–H is $\mathbf{2.6\, gcm^{-3}}$, the chemical formula is $(CaO)1.7\,(SiO_2)\,(H_2O)1.8$ and the $\boldsymbol{SLD}$ is $\mathbf{2.574 \cdot 10^{-14}\ m^{-2}}$. These values are used to compute the C–S–H/quartz refractive index and model the refraction caused by quartz at an interface with C–S–H.
The polarization resulting from refraction is the Fourier transform of Equation (4.5), which is given as:

$$\boldsymbol{P(B,\lambda) = \int_{\pi/2}^{-\pi/2} I(\theta) \cos(cL\theta B\lambda \cot\theta_0) d\theta} \tag{4.9}$$

The effect of multiple refractive layers in the neutron beam can be calculated by convolving the seperate contributions. Since a convolution in Fourier space corresponds to a multiplication in real space, the polarization for multiple identical refractive layers can be computed from the polarization of one layer as:

$$\boldsymbol{P(B,\lambda)_n = P(B,\lambda)^n} \tag{4.10}$$

where $\boldsymbol{n}$ is the number of layers.
In the case of a SESANS measurement, this angular distribution introduces a background to the perceived neutron scattering signal. In particular when multiple layers of refractive material are concerned, Plomp et al. [65] have shown that the effect can be destructive. Quartz particles present in concrete are not cylindrical.

They are encountered in shapes varying from angular to rounded and everything in between. Examples of these extremes are depicted in Fig. 4.5.

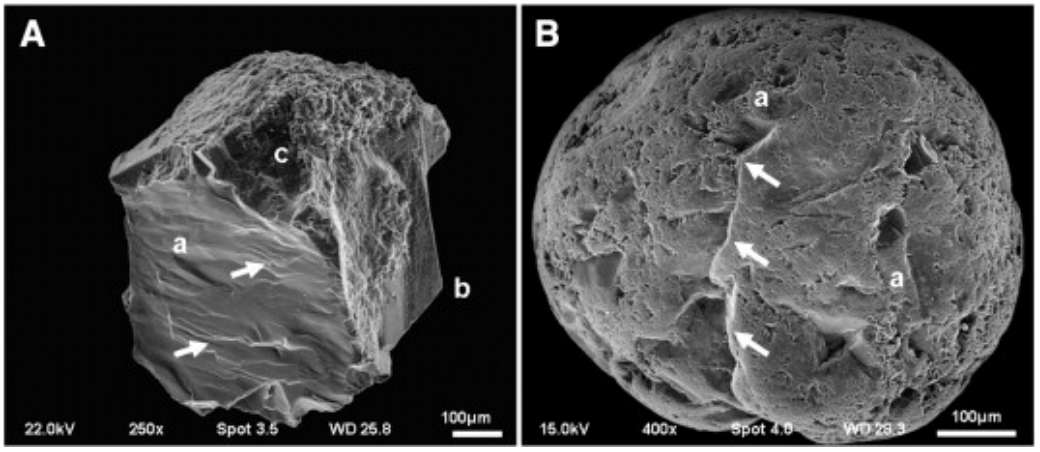

FIGURE 4.5: **Micrographs of quartz grains obtained by SEM in low vacuum mode and secondary electron mode.** After [67]. The used voltage, magnification, spot size and working distance (WD) are given in at the bottom of the pictures. The lower case letters and arrows may be neglected. **A** Angular grain with high relief. Origin: intertidal zone, Peninsula Fm, Ordovician, Cape Basin, South Africa. **B** Rounded grain with low to medium relief. Origin: braided river sediment, Pleistocene, Jaworzno, Poland.

Looking at these pictures it can be concluded that the shape of quartz particles is more effectively approached by a sphere than a cylinder. However, a model for the computation of the angular distribution caused by refraction in cylindrical wires is at hand and could be a starting point in estimating the contribution of refraction by quartz particles in SESANS measurements of concrete. When results indicate a significant distribution the further development of the model can be reconsidered.

Chapter 5

Experimental procedure

5.1 Preperation of concrete samples for SESANS measurements

The concrete samples used in this thesis are produced by COVRA (see Table 5.1 and were provided to us as cylinders in plastic casing (Figure 5.1).

Probing concrete samples by SESANS imposes a limit on the sample thickness. That is, the amount of scattering increases with increasing thickness and at some point, the number of detected neutrons will be insufficient for measurements. Therefore, the cylinders need to be cut into $1\boldsymbol{mm}$ disks.
Cutting is performed by making use of a Buehler IsoMet low speed saw (Figure 5.1).

An example of a concrete disk that was obtained by the procedure described above is shown in Figure 5.1e.

TABLE 5.1: **Recipe for the mortars produced by COVRA**.

Component	Specifications	Volume fraction (kg/m^3)
cement	CEM III/B 42.5 N LH/SR	408
water		143
superplasticizer	TM OFT-II B84/39 CON. 35% (BT-SPL)	4
foaming agent	mixed with water, ratio 80/23	5
fine aggregate	quartz sand 0-2mm	1121

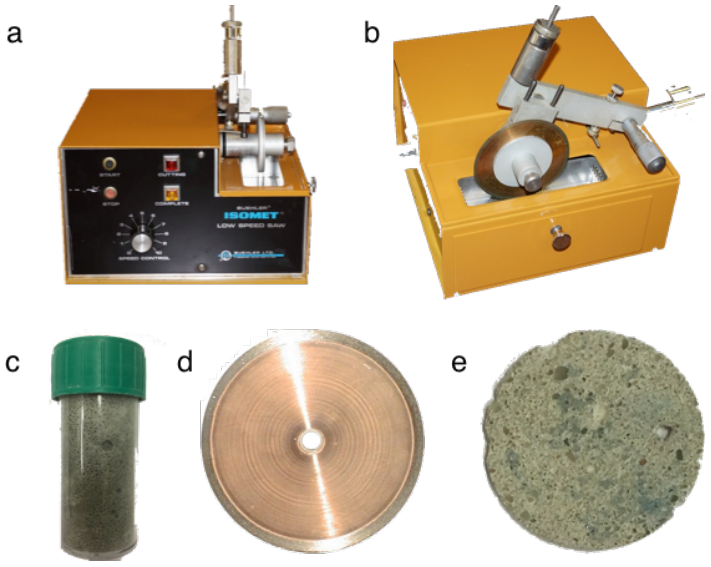

FIGURE 5.1: **Overview of the cutting process in images.** **a** Front view of the Buehler IsoMet low speed saw. On the lower left part of the image the knob which adjusts the speed can be seen. **b** Side view of the Buehler IsoMet low speed saw. In the middle of the image the copper wafering blade can be seen and just above that the weights that settle the downward force on the arm the the saw are visible. **c** The cylinder concrete sample encapsulated in plastic. **d** The IsoMet 15LC wafering blade. **e** One of the concrete disks that was prepared.

5.2 Concrete degradation

After cutting, the samples were immersed in solutions containing sulfates (4.1 g/L Na_2SO_4 and chlorides (29.8 g/L NH_4Cl as depicted in Fig. 5.2 to investigate the actions of degradation.

These concentrations were chosen in order to resemble the concentrations that are representative for the Rupel Member. Elevated concentrations in sulfate coincide with important concentrations in Ca and Mg coming from carbonate dissolution and cationic exchange which are caused by increasing of acidity due to pyrite oxidation [8]. The samples were stirred during the whole period of reaction (2 weeks and 2 months respectively) while the pH of solutions was checked periodically. At the end of each exposure time, samples were dried for at least 24 hours at 50-80°C, until a constant mass was obtained and placed independently in plastic bags and put in desiccator in order to preserve the samples and to prevent ulterior carbonation from the atmospheric CO_2. The concentrations used in these studies are close to the concentrations existing in the Dutch Boom clay pore water and seawater (Cl- 0.558 M, SO42- 0.0289 M). Ammonia ions and chlorides may have

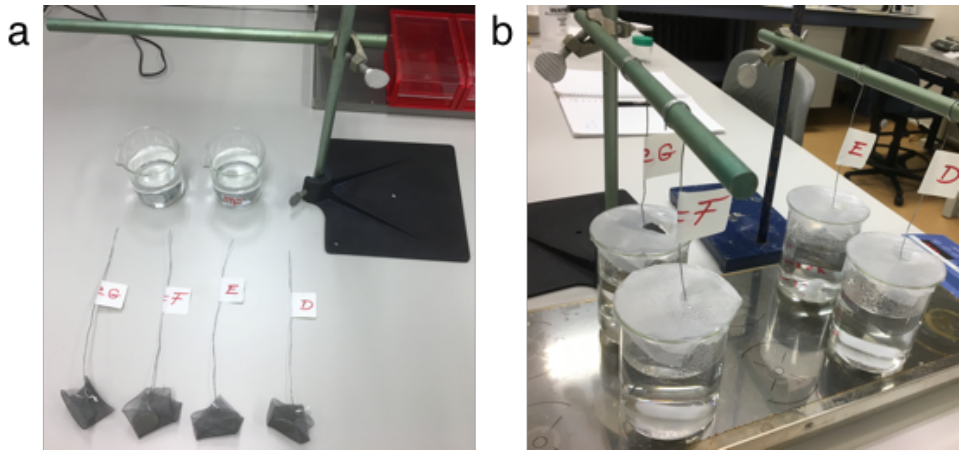

FIGURE 5.2: **Overview of the materials used in the degradation setup.** **a** The concrete disks were wrapped up in wire gauze, attached to iron wire and labeled with a letter. **b** The concrete disks were put in beakers with different solutions, covered by parafilm and placed on a stirring plate.

an important corrosion impact on concrete, causing pore increasing which may be suitable to be investigated at microscale by SESANS. In this study, the degraded and non-degraded samples will be compared.

5.3 Drying of concrete samples

Water is present in concrete in many physical states as discussed in [68]. These water molecules are causing neutron scattering in the concrete samples. One approach to investigate the effect of water on the depolarization measured by SESANS in concrete samples is to compare samples that are known to contain different amounts of water. Water can be removed from concrete by exposing it to higher temperatures. Drying of concrete at 50°C has been reported to remove water from the pores while causing minimal damage to the pore structure [68]. In these experiments some concrete samples have been dried at a temperature of 50°C for 12 hours.

5.4 Measurements on pure quartz

Table 5.1 shows that quartz occupies by far the largest volume fraction of the concrete. Samples consisting solely of quartz have been investigated as well to validate it's influence on the overall material. Observing Table 5.1 once more it

TABLE 5.2: **Description of the used quartz types.**

Name	Grain size (mm)	Supplier
Very fine	<0.1	Fluka Analytical
Fine	0.2 - 0.8	Boom Labaratoriumleverancier
Rough	0.4 - 0.8	Boom Labaratoriumleverancier
Very rough	1.0 - 2.0	Merck KGaA

TABLE 5.3: **Scattering length densities used in the model.**

Material	Molar mass ($\boldsymbol{kg/mol}$)	Mass density ($\boldsymbol{kg/m^3}$)	SLD ($Å^{-2}$)
$\mathbf{SiO_2}$	0.06008	2650	$\mathbf{4.168 \times 10^{14}}$
$\mathbf{C-S-H}$	0.18809	2604	$\mathbf{2.574 \times 10^{14}}$

can be seen that the grain sizes of the quartz particles cover a continuous range from $0\boldsymbol{mm}$ to $2\boldsymbol{mm}$. Therefore, four types of quartz with different grain sizes, given in Table 5.2, were chosen to represent this range. Now, with the cement missing as a paste binding all the quartz particles together, a sample holder need be installed. This consisted of two special quartzglasses, which neutrons can penetrate without being scattered, held together by ordinary adhesive tape. The tape was later cut away in the plain that would be transmitting neutrons, otherwise some neutron scattering by the tape would result in a background to the polarization measurements.

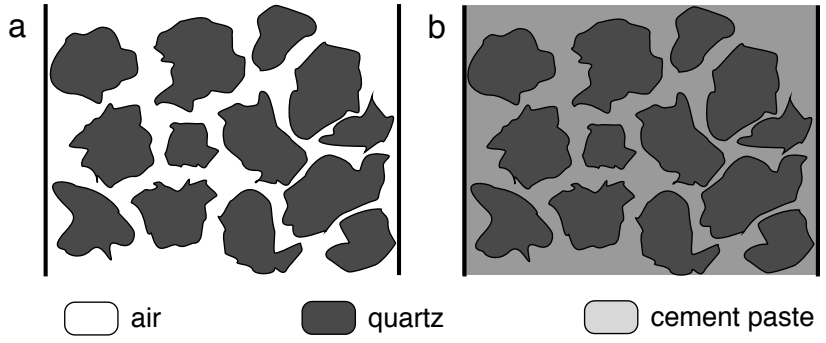

FIGURE 5.3: **Schematic of the interfaces occurring in pure quartz and concrete samples. a** Sample of pure quartz. **b** Sample of concrete, where the cement pasts is simplistically depicted as a homogenous phase.

In an oversimplified view the sample of pure quartz as depicted in Fig. 5.3 (a) can be compared to a sample of concrete as depicted in Fig. 5.3 (b) where the cement paste is subsituted by air. This results in a different SLD. The SLD values were obtained from the application by Kienzle and Brown which is accessible at the website of NIST Centre for Neutron Research [69] and are given in Table 5.3.

TABLE 5.4: **The mass densities and molar masses of the main components of concrete.** These data have been used to compute the scattering length densities that are possibly occurring in concrete. The volume percentages are an estimation on the basis of values presented in [47].

Component	Volume %		Molar mass (g/mol)	Density ($\boldsymbol{g/cm^3}$)
Quartz	64		60.08	2.65
C-S-H	33	18	74.08	2.60
CH		6	134.12	2.23
Ettringite		3	1255.11	1.78
Monosulfate		6	702.71	2.02
Mean value			136.44	2.52

The aforementioned application requires the input off the mass density of the substance and the conversion of SLD to mean coherent scattering length calls for the molar mass. Both are given in Table 5.4. The fact that the volume percentages in the second column of this table don't add up to 100% can be explained from a practical point of view. The neutron scattering density length calculator application by Kienzle and Brown requisites an input of chemical formulas that contain integer values only. Therefore, the numbers have been rounded off.

Chapter 6

Results & Discussion

In SESANS, the overall scatter of a substance depends on the scatter of all its components. Not only are there various components present in concrete, the structures of these are amorphous, complex and in some cases, even not agreed upon. Since quartz accounts for roughly 65% of the volume of concrete, a logical first step in the investigation of this seemingly inscrutable material is the isolated examination of its main component. Homogeneous phases that have structures relatively large compared to the wavelength of the neutrons might cause neutron refraction. Quartz is a mineral and thus can be classified as such a phase. Therefore, the analysis of SESANS data of concrete starts with an assessment of the significance of neutron refraction by quartz particles in SESANS measurements on pure quartz samples.

Quartz grains of many different sizes occur in concrete. Accordingly, quartz types of four different main grain sizes have been investigated by SESANS as shown in Fig. (6.1). Hence, this sample covers a size range from well below 0.1 mm to 2 mm. In Table 6.1 the fitted number of layers is compared with the number of layers that could geometrically fit in the sample holder based on the average grain size. The latter is essentially the thickness of the sample holder divided by the average grain size of a quartz sample.

Measurements agree remarkably well with the theoretically predicted model, indicating that refraction causes significant angular distribution of neutrons in SESANS measurements. But results should be called into question, because the assumed shape of the refracting elements differs excessively from reality. Still, the results clearly identify refraction as a phenomenon that must be taken into account in analyzing these measurements.

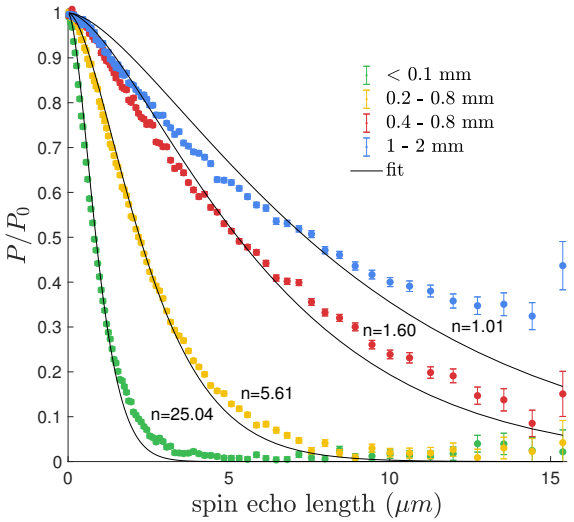

FIGURE 6.1: **Four types of quartz with different average grain size investigated by SESANS.** In all experiments a sample holder of 1.0 mm thickness was completely filled with the quartz grains leaving the unutilized space to be filled with air. The measurements are compared with the theoretical refraction model for cylinders by Plomp et al. [65] with the number of layers $\boldsymbol{n}$, appearing in Eq. (4.10), as the fitting parameter.

TABLE 6.1: A comparison of the theoretically expected $\boldsymbol{n_{th}}$ number of quartz layers with the experimentally observed number of layers $\boldsymbol{n_{ex}}$ and a display of the goodness of fit parameters for the obtained values of $\boldsymbol{n_{ex}}$.

Grain size (mm)	Goodness of fit			$\boldsymbol{n_{geo}}$	$\boldsymbol{n_{fit}}$
	SSE	R-square	RMSE		
<0.1	0.09176	0.9875	0.03408	20	25.04
0.2 - 0.8	0.06203	0.9934	0.02802	5	5.61
0.4 - 0.8	0.16160	0.9711	0.03762	2.5	1.60
1 - 2	0.37620	0.8843	0.0690	1	1.01

The next step is to estimate the extent to which neutron refraction by quartz particles contributes to the obtained SESANS signal in concrete. Pure quartz is stacked as an amorphous structure and therefore the packing factor can be approximated as:

$$\boldsymbol{\eta = \frac{\pi}{2} \simeq 0.63662} \tag{6.1}$$

Thus in a sample completely filled with quartz $\boldsymbol{\sim 64\%}$ of the volume is occupied by quartz particles and the remaining $\boldsymbol{\sim 36\%}$ by air. Now regarding concrete, aggregates typically occupy 60 - 75 % by volume of the concrete and the aggregates in this thesis consist completely of quartz. So, in a simplified model concrete could be compared to the pure quartz samples of the former experiment, but with the air replaced by cement paste. This cement paste, in turn, comprises **C−S−H**

as its most predominant component with a volume percentage of more than 50%. Furthermore, the C−S−H solid/pore interface dominates the interfacial surface area within hydrated cement [70]. Therefore, a sample of undegraded concrete is compared with the theoretical refraction model for the relative refractive index between quartz and C−S−H gel as depicted in Fig. (6.2). While not as preem-

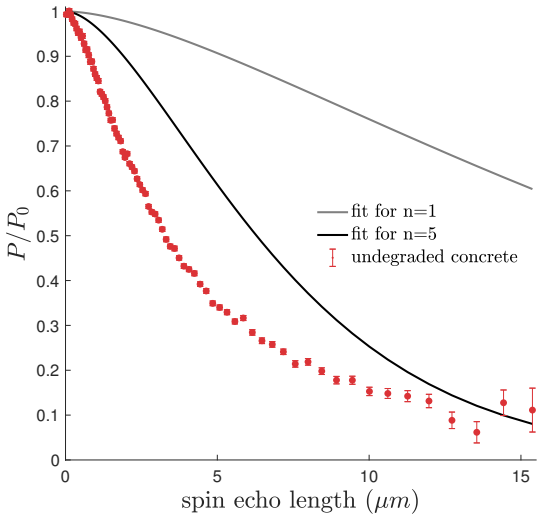

FIGURE 6.2: **Neutron polarization in concrete investigated by SESANS is compared to theoretically expected polarization due to refraction.** SESANS measurements on an undegraded concrete sample are represented by red dots. The sustained lines represent polarization due to refraction according to the theoretical refraction model for cylinders by Plomp et al. ([65]). The grey and black line assume a sample containing 1 layer and 5 layers of quartz particles in the direction of propagation of the neutron beam respectively. The relative refractive index for neutrons between quartz and C−S−H gel is used in the model.

inent as in pure quartz the phenomenon causes a significant background to the polarization. To draw meaningful conclusions from SESANS measurements on concrete the polarization should be corrected for this background. In the analysis of SESANS measurement data this can be done practically by dividing the normalized polarization measured in the concrete by the theoretically predicted contribution of refraction.

For the completeness of the stepwise analysis of concrete's most important components, measurements also have been performed on pure cement samples as depicted in Fig. (6.3). This figure shows that neutron diffraction in pure cement is much higher than in concrete. By comparing the initial slopes of both graphs the amount of scattering can be estimated to be 2.0 times higher in pure cement. This difference in amount of scattering can be explained largely by considering that concrete

consists for about 35% of cement paste. The pure cement sample thus contains roughly 3 times more cement paste than the concrete sample. Still, the quartz particles in the concrete sample disturb these measurements. As the samples were already cut to a thickness of only 1mm, further decreasing the sample thickness of the pure cement sample will be practically impossible. Producing samples that consist of 35% of cement paste and 65% of a substitute for quartz that does not cause depolarization of the neutrons by neither scattering nor refraction could be a suitable way to proceed. The question is, however, if such a substance exists.

Concrete is a heterogeneous material. Quartz particles and air-filled pores are

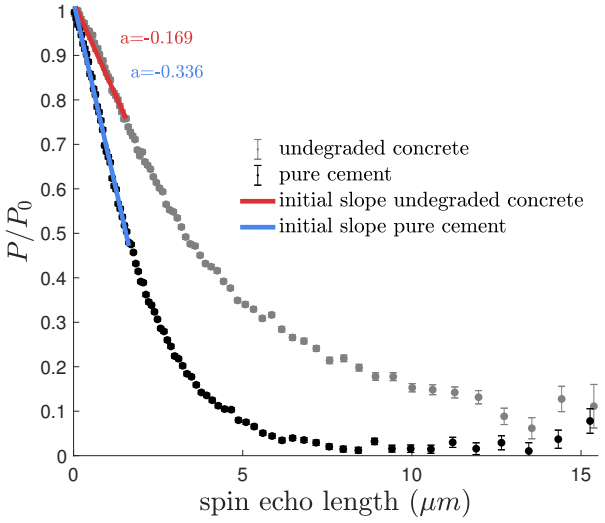

FIGURE 6.3: **A comparison of pure cement with concrete investigated by SESANS.** The pure cement sample is produced in the lab by mixing water with ENCI CEMI 42,5N cement in a w/c ratio of 0,45. The mix was poured into plastic cylinders and then cut in the exact same way and as the concrete samples. Also, samples of similar thickness were used. The red and blue lines represent the initial slopes of measurement curves for the undegraded concrete and pure cement respectively.

amorphously oriented in the cement paste, which itself is also heterogeneous. This gives rise to the question to what extent SESANS measurements are statistically reproducible for different concrete disks from the same batch. The results of SESANS measurements on these samples are displayed in Fig. (6.4). It shows that the normalized polarization caused by the different samples is almost exactly equal in a spin-echo length range from 0 to 12$\boldsymbol{\mu m}$. From this it can be concluded that the samples are large enough to obtain statistically meaningful results. The asserted reproducibility is very convenient for any further investigation of these samples. However, considering the vast complexity of the concrete structure and

the novelty of SESANS measurements on multi-componental substances, any far-reaching conclusions, based on this evidence solely, seem premature. On the other hand it could be mentioned that any heterogeneous substance can be considered as homogeneous if only the scale of interest is large enough.

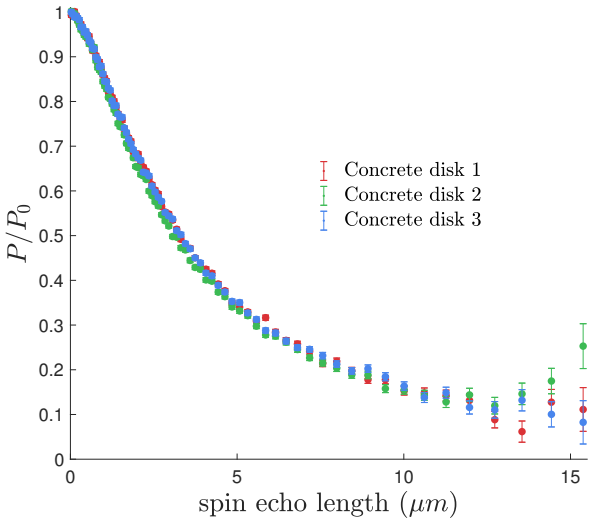

FIGURE 6.4: **SESANS measurements performed on different concrete disks cut out of cylinders from the same batch.** The three disks were cut from the middle of these different concrete cylinders. The concrete that was used is CEM III 42.5 N LH/SR

As discussed in the literature review section, water appears in concrete in many physical states. To get an impression of the influence of this water and its physical state on SESANS measurements, another measurement has been performed. One concrete disk has been dried at 50°C for 12 hours and another disk of the same batch has not been dried. Both have been measured with SESANS. The oven drying removed water from the sample. From Fig. (6.5) it can be seen that the depolarization in the dried sample is lower than in the sample that was not dried. The water molecules in the concrete are accountable for part of the neutron scattering. This implicates that the relative humidity in which the samples are kept might alter the measurement results. Samples should thus be kept at the exact same humidity conditions to be able to compare them. Another reason might exist for the decrease of scattering caused by drying the samples. The drying method involves the phase transformation of water from liquid to vapour. As this occurs, capillary suction is experienced which can induce micro-cracking and the collapse of the paste microstructure [71]. In any case, since the sample that has been oven dried was not the same sample as the sample that was not dried these results rely on the results of the reproducibility measurements.

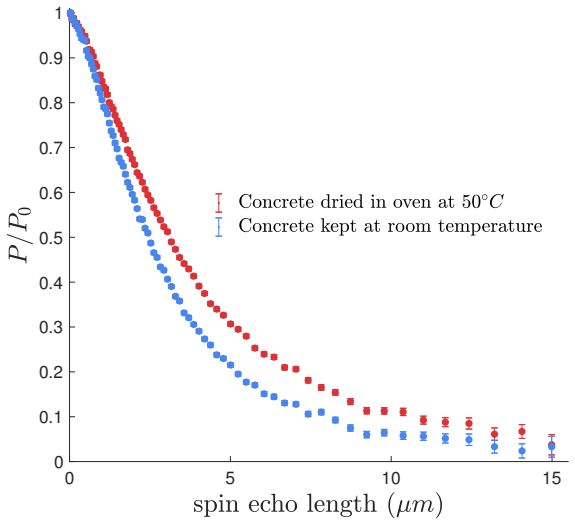

FIGURE 6.5: **A comparison of a dried concrete sample with a concrete sample that has not been dried by SESANS measurements.** Two concrete disks from the same batch were measured by SESANS. One was dried in the oven at 50°C for 12 hours and the other was kept in the desiccator at room temperature. Measurements have been performed in duplo, i.e. on two different spots of each disk (left and right).

As apparent from the results previously discussed there are still large gaps in the understanding of the data from SESANS measurements on concrete. The interpretation of such data with the aim of describing concrete porosity, would at least require a model that is able to recognize the pores. This level of progress has not yet been achieved. In Fig. (6.6) and Fig. (6.7) the results of SESANS measurements on samples, immersed in sodium sulfate and amonium chloride respectively, are depicted. For both chemical degradation mechanisms the data for the degraded samples clearly differ from the data for the undegraded samples. Moreover, they do so in an amount significantly larger than the measurement error encountered up to a spin-echo length of $\mathbf{12}\boldsymbol{\mu m}$. For the samples immersed in sodium sulfate the variation in duration of exposure does not reflect in the results. To the contrary, for the samples immersed in amoniumchloride the sample that was exposed for 2 weeks demonstrates less deviation from the undegraded sample than the sample that was exposed for 8 weeks. This could indicate a slower degradation process for the chloride ingress compared to sulfate attack.

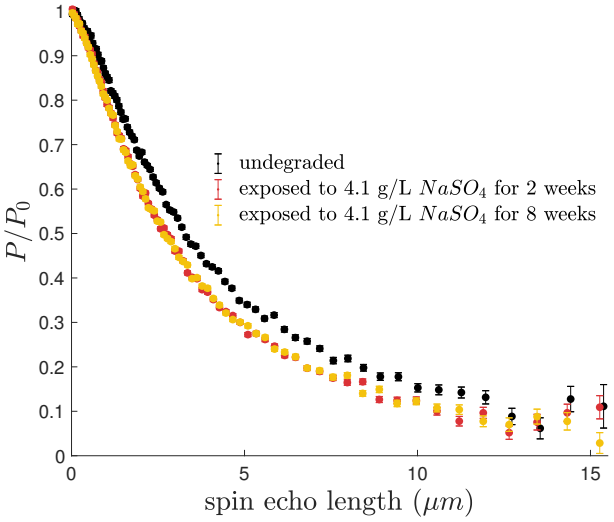

FIGURE 6.6: **An evaluation of the effect of immersing concrete disks in sodium sulfate solution.** The samples have been immersed for either 2 weeks or 8 weeks.

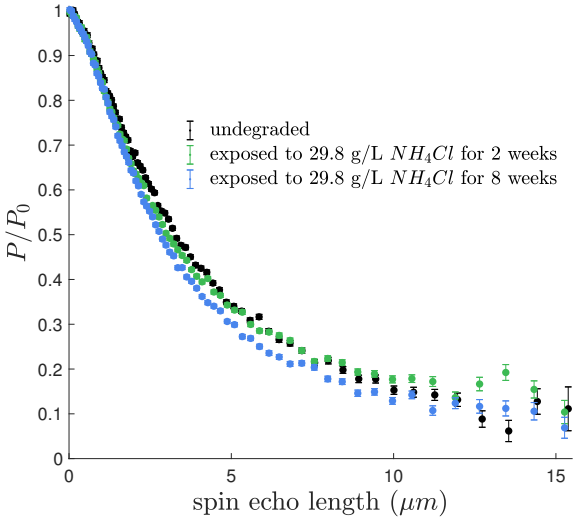

FIGURE 6.7: **An evaluation of the effect of immersing concrete disks in amoniumchloride solution.** The samples have been immersed for either 2 weeks or 8 weeks.

Chapter 7

Conclusions

In this thesis, it was explored whether SESANS can contribute to the investigation of the pore evolution in concrete due to degradation processes involving sulfates and chlorides, the main compounds of Boom Clay pore water. The investigation of pore evolution due to sulfate attack and chloride ingress has not yet been established because some difficulties were encountered. Neutron refraction by quartz particles causes a significant contribution to the signal measured by SESANS measurements on concrete. Any further quantitative analysis of such measurements should take this phenomenon into account. Drying the concrete prior to the measurement decreases the amount of scattering. This is presumably due to the removal of water molecules, which are accountable for part of the neutron scattering in the sample. Also, the associated collapse of the paste microstructure cannot be excluded as an explanation. Besides, reproducibility tests have shown that the sample dimensions are large enough to yield statistically consistent results. It can be concluded from the results that the effects of chemical degradation on concrete are perceptible in a scale significantly larger than the measurement error. Any further quantitative analysis of such measurements should take this phenomenon into account. The extensive removal of water by e.g. drying methods from the samples can contribute to the further elimination of parameters that blur the understanding of the obtained data. To gain more detailed information on the contribution of neutron refraction to the polarization a the refraction model must be modified to adjust for the amorphous form of the quartz particles, their anisotropical orientation and large variation in size.

Appendix A

Concrete: from cement to hydration products

Concrete is a composite material, which means that it is composed of more constituent materials that differ significantly in physical and chemical properties. When combined, the cement paste, which mainly consists of C-S-H gel, porlandite, ettringite, and monosulfate, bonds together the aggregate (quartz) to form new material (concrete) with qualities different than the individual components. This chapter regards the main elements of concrete, its hydration products and the chemical processes involved.

A.1 The production process of Portland cement

The raw materials needed to produce cement are limestone and clay or shale. They are extracted from quarry and crushed to a very fine powder. It is then blended in the correct proportions and thereafter called *kiln feed*. This is heated in a *rotary kiln* to temperatures of about $\mathbf{1400°C}$ to form *clinker*. After the cement mill grinds the clinker to fine powder and a small amount of gypsum is added, the substance is called *cement*.

TABLE A.1: **Abbreviation of the main oxides occurring in cementitious materials, according to the Cement Chemist Notation.** [72].

Oxide	Trivial name	Chemical formula	CCN
Calcium oxide	Lime	$\mathbf{CaO}$	$\mathbf{C}$
Silicon dioxice	Silica	$\mathbf{SiO_2}$	$\mathbf{S}$
Aluminum oxide	Alumina	$\mathbf{Al_2O_3}$	$\mathbf{A}$
Iron oxide	Rust	$\mathbf{Fe_2O_3}$	$\mathbf{F}$
Sulfur trioxide	-	$\mathbf{SO_3}$	$\mathbf{\overline{S}}$
Carbon dioxide	-	$\mathbf{CO_2}$	$\mathbf{\overline{C}}$

TABLE A.2: **Main clinker components.**

Compound	Trivial name	Chemical formula	CCN
Tricalcium silicate	Alite	$\mathbf{Ca_3SiO_5}$	$\mathbf{C_3S}$
Dicalcium silicate	Belite	$\mathbf{Ca_2SiO_4}$	$\mathbf{C_2S}$
Tricalcium aluminate	-	$\mathbf{Ca_3Al_2O_6}$	$\mathbf{C_3A}$
Tetracalcium alumino-ferrite	Fss	$\mathbf{Ca_2(Al_xFe_{1-x})_2O_5}$	$\mathbf{C_4AF}$
Calcium sulfate dihydrate	Gypsum	$\mathbf{CaSO_4 \cdot 2\,H_2O}$	$\mathbf{C\overline{S}H_2}$

A.2 Cement Chemistry Notation

In order to prevent the frequent use of tedious chemical notations, cement chemists use a more concise notation A.1. In Cement Chemist Notation (CCN) oxides are referred to by their first letter (e.g., C represents CaO). Several oxides that are most likely to occur in cementitious materials are given in Table A.1.

A.3 Mineral and oxide composition of Portland cement

Portland cement consists for more than 90% of the four main cement minerals: $\mathbf{C_3S}$ ($\sim$ **55%**), $\mathbf{C_2S}$ ($\sim$ **18%**), $\mathbf{C_3A}$ ($\sim$ **11%**) and $\mathbf{C_4AF}$ ($\sim$ **7%**). The names associated with these chemical formulas are given in Table A.2. Since the quarry from which the cement is made might differ vastly in composition the aforementioned percentages might fluctuate heavily between different samples.

The role of these minerals in the hydration process are very different. Almost all favourable properties are contributed by alite (C_3S) and belite (C_2S): they form the C-S-H gel. Reactivity differs among these two phases. Due to the asymmetric

packing of calcium and oxygen ions in their polymorphic structures larges holes are left in the crystal lattice. This causes the C_3S to have a higher internal energy than C_2S and thus the former is more reactive than the latter. Therefore, C_3S is responsible for the early strength. While the aluminate phase (C_3A) and the ferrite phase (C_4FA) are also subject to hydration, they contribute little to the beneficial properties of the cement paste. Their presence in cement is simply due to the fact that it's too costly to remove them [73]. In the presence of sulfate ions, C_3A might even damage the concrete by participating in expansive reactions that lead to stress and cracking. Moreover, C_4AF could represent a stable compound with any composition between C_2A and C_2F. All of the main clinker components are given in Table A.2.

A.4 The hydration of Portland cement

Concrete is produced by hydrating a mix of cement, sand and gravel. This hydration process involves many different reactions, of which the most important ones will be presented later on in this chapter.
The hydration of Portland cement is an exothermic reaction and therefore it can be represented by a calorimetric curve as in Figure A.1. Other experimental observations (e.g., the rate of release of $\mathbf{Ca^{2+}}$ ions into solution) could serve this purpose as well. Relative simplicity sensitivity and accuracy have made the calorimetric curve the most frequently used method [74].

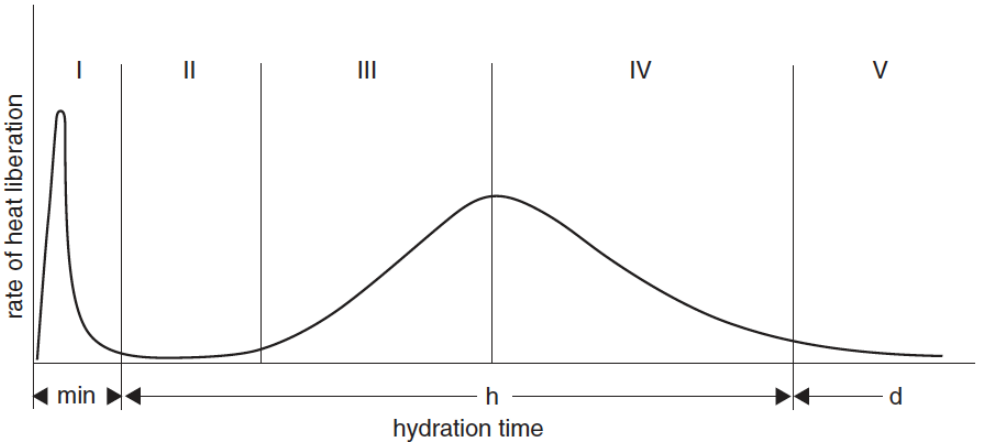

FIGURE A.1: After [75]. Schematic representation of heat evolution during hydration of a cement.

In the hydration process, the four major cement minerals react to form different solid phases at reaction rates that differ widely as well. The main hydration products will be discussed in the next subsections and are also shown in Table A.3.

TABLE A.3: **Main hydration products.** [72]

Compound	Trivial name	Chemical formula	CCN
Calcium hydroxide	Portlandite	$\mathbf{Ca(OH)_2}$	**CH**
Calcium silicate hydrate	-	$\mathbf{x CaO \cdot SiO_2 \cdot y H_2O}$	**C−S−H**
Calcium sulfate dihydrate	Gypsum	$\mathbf{CaSO_4 \cdot 2\,H_2O}$	$\mathbf{C\overline{S}H_2}$
Calcium aluminate monosulfate hydrate	Monosulfate (AFm)	$\mathbf{Ca_6Al_2(OH)_{12} \cdot SO_4 \cdot}$ $6\,H_2O$	$\mathbf{C_4A\overline{S}H_{12}}$
Calcium aluminate trisulfate hydrate	Ettringite (AFt)	$\mathbf{Ca_6Al_2(OH)_{12} \cdot (SO_4)_3 \cdot}$ $26\,H_2O$	$\mathbf{C_6A\overline{S}_3H_{32}}$
-	Thaumasite (AFt)	$\mathbf{Ca_3[Si(OH)_6]CO_3 \cdot SO_4 \cdot}$ $12\,H_2O$	$\mathbf{C_3S\overline{C}\overline{S}H_{15}}$

A.4.1 Tricalcium silicate (C_3S)

The hydradation of $\mathbf{C_3S}$ leads to the formation of calcium silicate hydrate and calcium hydrate (porlandite) as given in the following schematic equation:

$$\mathbf{2\,C_3S + 6\,H \longrightarrow C_3S_2H_3 + 3\,CH} \tag{A.1}$$

A.4.2 Dicalcium silicate (C_2S)

In the case of $\mathbf{C_2S}$ we speak of hydrolysis rather than hydration, but otherwise the reaction occurs analogously as with $\mathbf{C_3S}$ and the reaction can be schematically represented as:

$$\mathbf{2\,C_2S + 4\,H \longrightarrow C_3S_2H_3 + CH} \tag{A.2}$$

Although the reaction products are the same, the relative amount of **CH** is three times lower. Furthermore, the reaction rate is much lower due to the lower solubility of $\mathbf{C_2S}$ in water compared to $\mathbf{C_3S}$. The $\mathbf{C_2S}$ thus contributes little to the early strength of cement, but plays an important role in providing strength to the mature cement paste and concrete.

A.4.3 Caclium aluminates (C_3A)

The hydration reaction of $\mathbf{C_3A}$ occurs in different forms dependent on the presence of sulfate ions in the pore solution. Reaction with pure water results in the following sequence:

$$\mathbf{2\,C_3A + 21\,H \longrightarrow C_4A_{19} + C_2AH_8 \longrightarrow 2\,C_3AH_6 + 9\,H} \tag{A.3}$$

where the first reaction rate is very high and the second reaction takes place rather slowly. The high reaction rate and exothermic character of the first reaction would cause the paste to set within a few minutes. This loathsome phenomenon is called *flash set*. It can be prevented by adding gypsum ($\mathbf{C\overline{S}H_2}$) to the cement mix. Due to its high solubility gypsum will immediately release sulfate ions which react with the $\mathbf{C_3A}$ to form ettringite:

$$\mathbf{C_3A + 3\,C\overline{S}H_2 + 26\,H \longrightarrow C_6A\overline{S}_3H_{32}} \tag{A.4}$$

When all gypsum has reacted but there's still $\mathbf{C_3A}$ left, then yet another reaction might occur:

$$\mathbf{2\,C_3A + C_6A\overline{S}_3H_{32} + 4\,H \longrightarrow 3\,C_4A\overline{S}H_{12}} \tag{A.5}$$

Since gypsum is always added to cement the $\mathbf{C_3A}$ mainly reacts according to eqs. A.4 and eqs. A.5 and A.3 only occur exceptionnaly.

A.4.4 Calcium ferrites (C_4AF)

The hydration ($\mathbf{C_4AF}$) is similar to the reactions described above (eqs. A.4 and A.5) for the aluminate phase, but with a lower reaction rate. An important phenomenon that occurs here is the partial substitution of aluminum ions by iron ions. The reaction can be expressed schematticaly as:

$$\mathbf{C_4AF + 3\,C\overline{S}H_2 + 21\,H \longrightarrow C_6(A,F)\overline{S}_3H_{32} + (F,A)H_3} \tag{A.6}$$

$$\mathbf{C_4AF + C_6(A,F)\overline{S}_3H_{32} + 7\,H \longrightarrow 3\,C_4(A,F)\overline{S}H_{12} + (F,A)H_3} \tag{A.7}$$

where (A,F) indicates aluminum with variable substitution of iron, and (F,A) indicates iron with variable substitution of aluminum. Due to this substitution, the main reaction products have the same crystal structures but aren't exactly

TABLE A.4: Summary of the main reactants in the hydration process and the associated reaction products.

Reactant	Reaction products
$\mathbf{C_3S}$ (alite)	**CH**, **C−S−H**
$\mathbf{C_2S}$ (belite)	**CH**, **C−S−H**
$\mathbf{C_3A}$	Ettringite, monosulfate
$\mathbf{C_4AF}$ (Fss)	Ettringite, monosulfate
C (free lime)	**CH**
Ettringite	Monosulfate

ettringite and monosulfoaluminate. Therefore, they are given the names *AFt* and *AFm*, where the *t* implies trisulfate and the *m* implies monosulfate. These abbreviations are commonly used in cement chemistry, because when $\mathbf{C_3A}$ and $\mathbf{C_2A}$ are well mixed in a cement there will always be some iron present in the reaction products which contain aluminum.

A.5 Hydration products

The main hydration products of Portland cement will be discussed below and are also shown in Table A.4.

A.5.1 Calcium silicate hydrate (C−S−H)

The C-S-H gel determines the basic properties of Portland cement pastes and occupies 50% of the paste volume [76]. Unsurprisingly, this phase is the subject of plentiful investigations [77]. From this we know that there exist a distinction between low-density and high density $\mathbf{C-S_H}$ [78]. The former of which is essentially formed during the early hydration stages and seems to occupy the spaces that were at first repleted by water. While the latter is predominantly formed during later hydration stages and occupies the spaces that were at first taken by the cement particles.

Rather than being intrinsically strong or stable **C−S−H** contributes to the concrete strength by providing cohesion to the cement particles as a continuous gel. Inversely, most of the other hydration products are intrinsically strong, but lack in cohesion with neighbouring particles.

A.5.2 Calcium hydroxide (CH)

In the hydration process, as **CH** forms as crystals in wide-ranging shapes and sizes, liquid water is transformed into solid form, thereby providing strength and impermeability to the paste. Nonetheless, this phase is not as relevant in terms of strength contribution as **C−S−H** and also only makes up about 15% of the total paste volume. It's presence in the paste entails some threatening downsides as well. Specifically, from all hydration products **CH** is the most soluble and thus will be susceptible to leaching.

A.5.3 Calcium sulfoaluminate phases (AFm an AFt)

As explained in paragraph A.4.3 and A.4.4 the hydration products of $\mathbf{C_3A}$ and $\mathbf{CA_4F}$ are calcium sulfoaluminate ettringite and monosulfate respectively. These phases have very different morphologies, but in most cases the crystals formed are small. In accordance with **CH**, these reaction products are also characterized by a minimal strength contribution that comes along with an increased exposure to external attacks. In this case sulfate attack is the main culprit.

The hydration products that form from the C3A and C4AF minerals occupy about 15-25% of the volume of a mature portland cement paste. As with CH, they do not contribute much to the engineering properties of concrete, except in a negative sense when a cement paste undergoes sulfate attack.

Bibliography

[1] Grupa. Report on the safety assessment methodology. *OPERA-PU-NRG2121*, April 2014.

[2] Grupa Poley Verhoef, Neeft. Outline of a disposal concept in clay. *Opera*, November 2014.

[3] S. Diamond. Aspects of concrete porosity revisited. *Cement and Concrete Research*, 29(8):1181–1188, 1999.

[4] Jacques D. Seetharam, S. Potential degradation processes of the cementitious ebs components, their potential implications on safety functions and conceptual models for quantitative assessment. *OPERA-PU-SCK514*, July 2015.

[5] M. Koenen and J Griffioen. Characterisation of the geochemical heterogeneity of the rupel clay member in the netherlands. *Netherlands Journal of Geosciences*, 95(3):269–281, 2016.

[6] J. Boisson. Clay club catalogue of characteristics of argillaceous rocks. *OECD Publicatioins*, pages 27–72, April 2005.

[7] M. Koenen and J. Griffioen. Report on mineralogical and geochemical characterization of boom clay. *OPERA-PU-TNO521-1*, November 2014.

[8] T. Behrends, I. van der Veen, A. Hoving, and J. Griffioen. First assessment of the pore water composition of Rupel Clay in the Netherlands and the characterisation of its reactive solids. *Netherlands Journal of Geosciences*, 95 (3):315–335, 2016.

[9] T. Behrends and C. Bruggeman. Determining redox properties of clay-rich sedimentary deposits in the context of performance assessment of radioactive

waste repositories: Conceptual and practical aspects. *OPERA-PU-UTR611-1*, June 2016.

[10] Tomas Ekström. *Leaching of concrete: the leaching process and its effects.* PhD thesis, LTH, Lund University, 2003.

[11] Thomas Dyer. *Concrete Durability*, chapter 3, pages 99–182. 2014. ISBN 978-0-415-56475-5.

[12] G. Escadeillas and H. Hornain. The durability of concretes: the concrete durability with respect to the chemically aggressive environments. *Vichot Scientific basis for the formulation of concretes durable in their environment. Presses ENPC*, 2008.

[13] B. Lagerblad. Leaching performance of concrete based on studies of samples from old concrete constructions. Technical Report SKB-TR–01-27, Swedish nuclear fuel and waste management company, 2001.

[14] K Yokozeki, K Watanabe, N Sakata, and N Otsuki. Modeling of leaching from cementitious materials used in underground environment. *Applied clay science*, 26(1):293–308, 2004.

[15] D. Jacques and D. Mallants. Evolution of concrete pore water and solid phase composition during leaching with different types of water. *NIROND-TR*, 24: V2, 2008.

[16] A. Burnol and P. Blanc. Uncertainty in the reactive transport model response to an alkaline perturbation in a clay formation. 2006.

[17] Laurent Trotignon, Hugues Peycelon, and Xavier Bourbon. Comparison of performance of concrete barriers in a clayey geological medium. *Physics and Chemistry of the Earth, Parts A/B/C*, 31(10):610–617, 2006.

[18] L Trotignon, V Devallois, H Peycelon, C Tiffreau, and X Bourbon. Predicting the long term durability of concrete engineered barriers in a geological repository for radioactive waste. *Physics and Chemistry of the Earth, Parts A/B/C*, 32(1):259–274, 2007.

[19] Josep M Soler. Reactive transport modeling of the interaction between a high-ph plume and a fractured marl: the case of wellenberg. *Applied geochemistry*, 18(10):1555–1571, 2003.

[20] Sanheng Liu, Diederik Jacques, Joan Govaerts, and Lian Wang. Conceptual model analysis of interaction at a concrete–boom clay interface. *Physics and Chemistry of the Earth, Parts A/B/C*, 70:150–159, 2014.

[21] Zijian Song, Linhua Jiang, and Hongqiang Chu. Impact of calcium leaching on chloride diffusion behavior of cement pastes exposed to ammonium chloride aqueous solution. *Construction and Building Materials*, 153:211–215, 2017.

[22] R. Pabalan, F. Glasser, and D. Pickett. *Review of literature and assessment of factors relevant to performance of groutedsystems for radioactive waste disposal*. Center for Nuclear Waste Regulatory Analyses, San Antonio, Texas, 2009.

[23] M. Santhanam, M. Cohen, and J. Olek. Mechanism of sulfate attack: A fresh look: Part 1: Summary of experimental results. *Cement and Concrete Research*, 32(6):915 – 921, 2002. ISSN 0008-8846.

[24] J. Skalny, J. Marchand, and I. Odler. *Sulfate Attack on Concrete*. Spon Press, 2002. ISBN 0–419–24550-2.

[25] A Neville. The confused world of sulfate attack on concrete. *Cement and Concrete Research*, 34(8):1275 – 1296, 2004. ISSN 0008-8846.

[26] A. Soive, E. Roziere, and A. Loukili. Parametrical study of the cementitious materials degradation under external sulfate attack through numerical modeling. *Construction and Building Materials*, 112:267 – 275, 2016. ISSN 0950-0618.

[27] J. Stroh, B. Meng, and F. Emmerling. Monitoring of sulphate attack on hardened cement paste studied by synchrotron xrd. *Solid State Sciences*, 48: 278 – 285, 2015. ISSN 1293-2558.

[28] T. Schmidt, B. Lothenbach, M. Romer, K. Scrivener, D. Rentsch, and R. Figi. A thermodynamic and experimental study of the conditions of thaumasite formation. *Cement and Concrete Research*, 38(3):337–349, 2008.

[29] D. Min and T. Mingshu. Formation and expansion of ettringite crystals. *Cement and concrete research*, 24(1):119–126, 1994.

[30] B. Tian and M. Cohen. Does gypsum formation during sulfate attack on concrete lead to expansion? *Cement and Concrete Research*, 30(1):117–123, 2000.

[31] M. Santhanam, M. Cohen, and J. Olek. Effects of gypsum formation on the performance of cement mortars during external sulfate attack. *Cement and Concrete Research*, 33(3):325–332, 2003.

[32] B. Mather. Discussion of "the process of sulfate attack on cement mortars" by shen yang, xu zhongzi, and tang mingshu. *Advanced Cement Based Materials*, 5(3):109–110, 1997.

[33] Thomas Schmidt, Barbara Lothenbach, Michael Romer, Karen Scrivener, Daniel Rentsch, and Renato Figi. A thermodynamic and experimental study of the conditions of thaumasite formation. *Cement and Concrete Research*, 38(3):337–349, 2008.

[34] N. Crammond. The thaumasite form of sulfate attack in the UK. *Cement and Concrete Composites*, 25(8):809–818, 2003.

[35] Adam Neville. Chloride attack of reinforced concrete: an overview. *Materials & Structures*, 28(2):63, 1995. ISSN 1359-5997. doi: 10.1007/BF02473172.

[36] E. Poulsen and L. Mejlbro. *Diffusion of Chloride in Concrete: Theory and Application*. CRC Press, Taylor & Francis Group, 2005. ISBN 9780419253006.

[37] Fabien Barberon, Vronique Baroghel-Bouny, Hlne Zanni, Bruno Bresson, Jean-Baptiste d'Espinose de la Caillerie, Lucie Malosse, and Zehong Gan. Interactions between chloride and cement-paste materials. *Magnetic Resonance Imaging*, 23(2):267 – 272, 2005. ISSN 0730-725X. doi: http://dx.doi.org/10.1016/j.mri.2004.11.021.

[38] V.G. Papadakis. Effect of supplementary cementing materials on concrete resistance against carbonation and chloride ingress. *Cement and concrete research*, 30(2):291–299, 2000.

[39] M. Torres-Luque, E. Bastidas-Arteaga, F. Schoefs, M. Sánchez-Silva, and J.F. Osma. Non-destructive methods for measuring chloride ingress into concrete: State-of-the-art and future challenges. *Construction and Building Materials*, 68:68–81, 2014.

[40] J Inacio, C Taviot-Guho, C Forano, and J.P Besse. Adsorption of mcpa pesticide by mgal-layered double hydroxides. *Applied Clay Science*, 18(5):255 – 264, 2001. ISSN 0169-1317. doi: http://dx.doi.org/10.1016/S0169-1317(01)00029-1.

[41] A. Terzis, H. Filippakis, S. Kuzel, and Hans Burzlaff. The crystal structure of ca2al(oh)6cl 2h2o. *Zeitschrift fr Kristallographie - Crystalline Materials*, 181(1–4):29–34, 1987. ISSN 21967105. doi: 10.1524/zkri.1987.181.14.29.

[42] A.K. Suryavanshi, J.D. Scantlebury, and S.B. Lyon. Mechanism of friedel's salt formation in cements rich in tri-calcium aluminate. *Cement and Concrete Research*, 26(5):717 – 727, 1996. ISSN 0008-8846. doi: http://dx.doi.org/10.1016/S0008-8846(96)85009-5.

[43] James V Bothe and Paul W Brown. PhreeqC modeling of friedel's salt equilibria at 231 C. *Cement Concrete Res*, 34(6):1057–1063, 2004. ISSN 0008-8846. doi: 10.1016/j.cemconres.2003.11.016.

[44] Birnin-Yauri, U.A and F.P Glasser. Friedels salt, Ca2Al(OH)6(Cl,OH)·2H2O: its solid solutions and their role in chloride binding. *Cement Concrete Res*, 28 (12):1713–1723, 1998. ISSN 0008-8846. doi: 10.1016/S0008-8846(98)00162-8.

[45] R. Kumar and B Bhattacharjee. Porosity, pore size distribution and in situ strength of concrete. *Cement and concrete research*, 33(1):155–164, 2003.

[46] C. Gallé. Effect of drying on cement-based materials pore structure as identified by mercury intrusion porosimetry: a comparative study between oven-, vacuum-, and freeze-drying. *Cement and Concrete Research*, 31(10):1467–1477, 2001.

[47] P.K. Mehta. *Concrete: structure, properties, and materials*. PTR Prentice-Hall, 1986. ISBN 0131671154 9780131671157.

[48] V.S. Ramachandran and J.J. Beaudoin. *Handbook of analytical techniques in concrete science and technology: principles, techniques and applications*. Elsevier, 2000. ISBN 0–8155–1473–9.

[49] F. Sanchez and K. Sobolev. Nanotechnology in concrete; a review. *Construction and Building Materials*, 24(11):2060 – 2071, 2010.

[50] I.G. Richardson. Tobermorite/jennite-and tobermorite/calcium hydroxide-based models for the structure of CSH: applicability to hardened pastes of tricalcium silicate, β-dicalcium silicate, Portland cement, and blends of Portland cement with blast-furnace slag, metakaolin, or silica fume. *Cement and Concrete Research*, 34(9):1733–1777, 2004.

[51] X. Cong and R.J. Kirkpatrick. 29Si MAS NMR study of the structure of calcium silicate hydrate. *Advanced Cement Based Materials*, 3(3-4):144–156, 1996.

[52] J. Skibsted and C. Hall. Characterization of cement minerals, cements and their reaction products at the atomic and nano scale. *Cement and Concrete Research*, 38(2):205–225, 2008.

[53] H.N. Bordallo, L.P. Aldridge, and A. Desmedt. Water dynamics in hardened ordinary Portland cement paste or concrete: from quasielastic neutron scattering. *The Journal of Physical Chemistry B*, 110(36):17966–17976, 2006.

[54] H.M. Jennings. Refinements to colloid model of C–S–H in cement: CM-II. *Cement and Concrete Research*, 38(3):275–289, 2008.

[55] M. Rekveldt, W. Bouwman, and W. Kraan. *Elastic Neutron Scattering Measurements Using Larmor Precession of Polarized Neutrons*, pages 87–99. Springer Berlin Heidelberg, Berlin, Heidelberg, 2003. ISBN 978-3-540-45823-4. doi: 10.1007/3-540-45823-9_9. URL http://dx.doi.org/10.1007/3-540-45823-9_9.

[56] D.L. Price and K. Skold. Introduction to neutron scattering. *Methods of Experimental Physics*, 23A, 1986.

[57] David L Price and Kurt Skold. Methods in experimental physics. pages 1–97, 1986. ISSN 0076-695X. doi: 10.1016/S0076-695X(08)60554-2.

[58] Ferenc Mezei. The principles of neutron spin echo. In F. Mezei, editor, *Neutron Spin Echo*, chapter 1, pages 1–26. Springer Berlin Heidelberg, Grenoble Cdex, France, 1980.

[59] V Bargmann, Louis Michel, and VL Telegdi. Precession of the polarization of particles moving in a homogeneous electromagnetic field. *Phys Rev Lett*, 2 (10):435–436, 1959. ISSN 0031-9007. doi: 10.1103/PhysRevLett.2.435.

[60] R Gähler, R Golub, K Habicht, T Keller, and J Felber. Space-time description of neutron spin echo spectrometry. *Phys B Condens Matter*, 229(1):1–17, 1996. ISSN 0921-4526. doi: 10.1016/S0921-4526(96)00509-1.

[61] Wim G Bouwman, Jeroen Plomp, Victor O de Haan, Wicher H Kraan, Ad A van Well, Klaus Habicht, Thomas Keller, and Theo M Rekveldt. Real-space

neutron scattering methods. 586(1):9–14, 2008. ISSN 0168-9002. doi: 10.1016/j.nima.2007.11.045.

[62] Theo M Rekveldt, Jeroen Plomp, Wim G Bouwman, Wicher H Kraan, Serguei Grigoriev, and Menno Blaauw. Spin-echo small angle neutron scattering in delft. *Rev Sci Instrum*, 76(3):033901, 2005. ISSN 0034-6748. doi: 10.1063/1.1858579.

[63] Robert Andersson, Léon F. van Heijkamp, Ignatz M. de Schepper, and Wim G. Bouwman. Analysis of spin-echo small-angle neutron scattering measurements. *Journal of Applied Crystallography*, 41(5):868–885, Oct 2008. doi: 10.1107/S0021889808026770. URL https://doi.org/10.1107/S0021889808026770.

[64] Timofei Krouglov, Ignatz M. de Schepper, Wim G. Bouwman, and M. Theo Rekveldt. Real-space interpretation of spin-echo small-angle neutron scattering. *Journal of Applied Crystallography*, 36(1):117–124, Feb 2003. doi: 10.1107/S0021889802020368. URL https://doi.org/10.1107/S0021889802020368.

[65] J. Plomp, J.G. Barker, V.O. De Haan, W.G. Bouwman, and A.A. van Well. Neutron refraction by cylindrical metal wires. *Nuclear Instruments and Methods in Physics*, 574(2):324–329, 2007.

[66] A.J. Allen, J.J. Thomas, and H.M. Jennings. Composition and density of nanoscale calcium-silicate-hydrate in cement. *Nature materials*, 6(4):311, 2007.

[67] K. Vos, N. Vandenberghe, and J. Elsen. Surface textural analysis of quartz grains by scanning electron microscopy (SEM): From sample preparation to environmental interpretation. *Earth-Science Reviews*, 128:93–104, 2014.

[68] Z. Mukadam, M.G. Alexander, and H.D. Beushausen. The effect of drying preconditioning on the South African durability index tests. *Cement and Concrete Composites*, 69:1–8, 2016.

[69] Paul Kienzle and David Brown. Neutron activation and scattering calculator, May 2017. URL https://www.ncnr.nist.gov/resources/activation/.

[70] A.J. Allen and J.J. Thomas. Analysis of C–S–H gel and cement paste by small-angle neutron scattering. *Cement and Concrete Research*, 37(3):319–324, 2007.

[71] J. Zhang and G.W. Scherer. Comparison of methods for arresting hydration of cement. *Cement and Concrete Research*, 41(10):1024–1036, 2011.

[72] S.N. Ghosh. *Cement and Concrete Science and Technology*. Thomas Telford, 1991.

[73] H. Taylor. *Cement Chemistry*. Academic Press, 1990. ISBN 0-12-683900-X.

[74] E.M. Gartner, J.F. Young, D.A. Damidot, and I. Jawed. Hydration of portland cement. In J. Bensted and Barnes. P., editors, *Structure and Performance of Cements*, chapter 3, pages 57–108. Spon Press, London, 2002.

[75] E.M. Gartner, J.F. Young, D.A. Damidot, and I. Jawed. Hydration of portland cement. *Structure and performance of cements*, 13:978–0, 2002.

[76] W. Kurdowski. *Cement and Concrete Chemistry*. Springer, 2014. ISBN 978-94-007-7944-0. doi: 10.1007/978-94-007-7945-7.

[77] H. Taylor. 8th ICCC Rio de Janeiro, vol. i. *Rio de Janeiro*, 1986.

[78] I.G. Richardson. The nature of C-S-H in hardened cements. *Cement and Concrete Research*, 29(8):1131–1147, 1999.